

Cross-scale energy transfer from fluid-scale Alfvén waves to kinetic-scale ion acoustic waves in the Earth’s magnetopause boundary layer

Xin An,^{1,*} Anton Artemyev,¹ Vassilis Angelopoulos,¹
Terry Z. Liu,¹ Ivan Vasko,² and David Malaspina^{3,4}

¹*Department of Earth, Planetary, and Space Sciences,
University of California, Los Angeles, CA, 90095, USA*

²*Department of Physics, University of Texas at Dallas, Richardson, TX, 75080, USA*

³*Astrophysical and Planetary Sciences Department,
University of Colorado, Boulder, CO, 80305, USA*

⁴*Laboratory for Atmospheric and Space Physics,
University of Colorado, Boulder, CO, 80303, USA*

(Dated: November 27, 2024)

Abstract

In space plasmas, large-amplitude Alfvén waves can drive compressive perturbations, accelerate ion beams, and lead to plasma heating and the excitation of ion acoustic waves at kinetic scales. This energy channelling from fluid to kinetic scales represents a complementary path to the classical turbulent cascade. Here, we present observational and computational evidence to validate this hypothesis by simultaneously resolving the fluid-scale Alfvén waves, kinetic-scale ion acoustic waves, and their imprints on ion velocity distributions in the Earth’s magnetopause boundary layer. We show that two coexisting compressive modes, driven by the magnetic pressure gradients of Alfvén waves, not only accelerate the ion tail population to the Alfvén velocity, but also heat the ion core population near the ion acoustic velocity and generate Debye-scale ion acoustic waves. Thus, Alfvén-acoustic energy channeling emerges as a viable mechanism for plasma heating near plasma boundaries where large-amplitude Alfvén waves are present.

* phyax@ucla.edu; <https://sites.google.com/view/xin-an-physics>

Understanding the multiscale energy transfer from magnetohydrodynamic electromagnetic perturbations and convective flows to kinetic field structures and plasma heating is of crucial importance in space and many other plasmas. The classical picture suggests that turbulent energy cascades from large to successively smaller scales through nonlinear interactions between counter-propagating Alfvén waves [1–5]. A complementary path of energy transfer involves the electrostatic coupling between Alfvénic and ion acoustic fluctuations. In this scenario, magnetic pressure gradients of Alfvén waves induce density perturbations and electric fields parallel to the background magnetic field [e.g., 6], which accelerate ion beams through nonlinear Landau resonance [7–9]. These ion beams then excite kinetic-scale ion acoustic waves (IAWs), which in turn relax ion beams, leading to parallel ion heating and terminating the energy transfer [10–13]. The implications of Alfvén-acoustic channeling on multiscale energy transfer span across space, astrophysical, and fusion plasmas. In the solar wind, IAWs and associated ion beams are observed around magnetic discontinuities or switchbacks [14–17], which likely evolve from outward-propagating Alfvén waves [18–20], resulting in significant ion heating [21–23]. In Tokamak plasmas, Alfvén waves driven by suprathermal ions transfer some of their energy to IAWs, which are heavily Landau-damped by thermal ions, thereby heating the thermal ions [24–27].

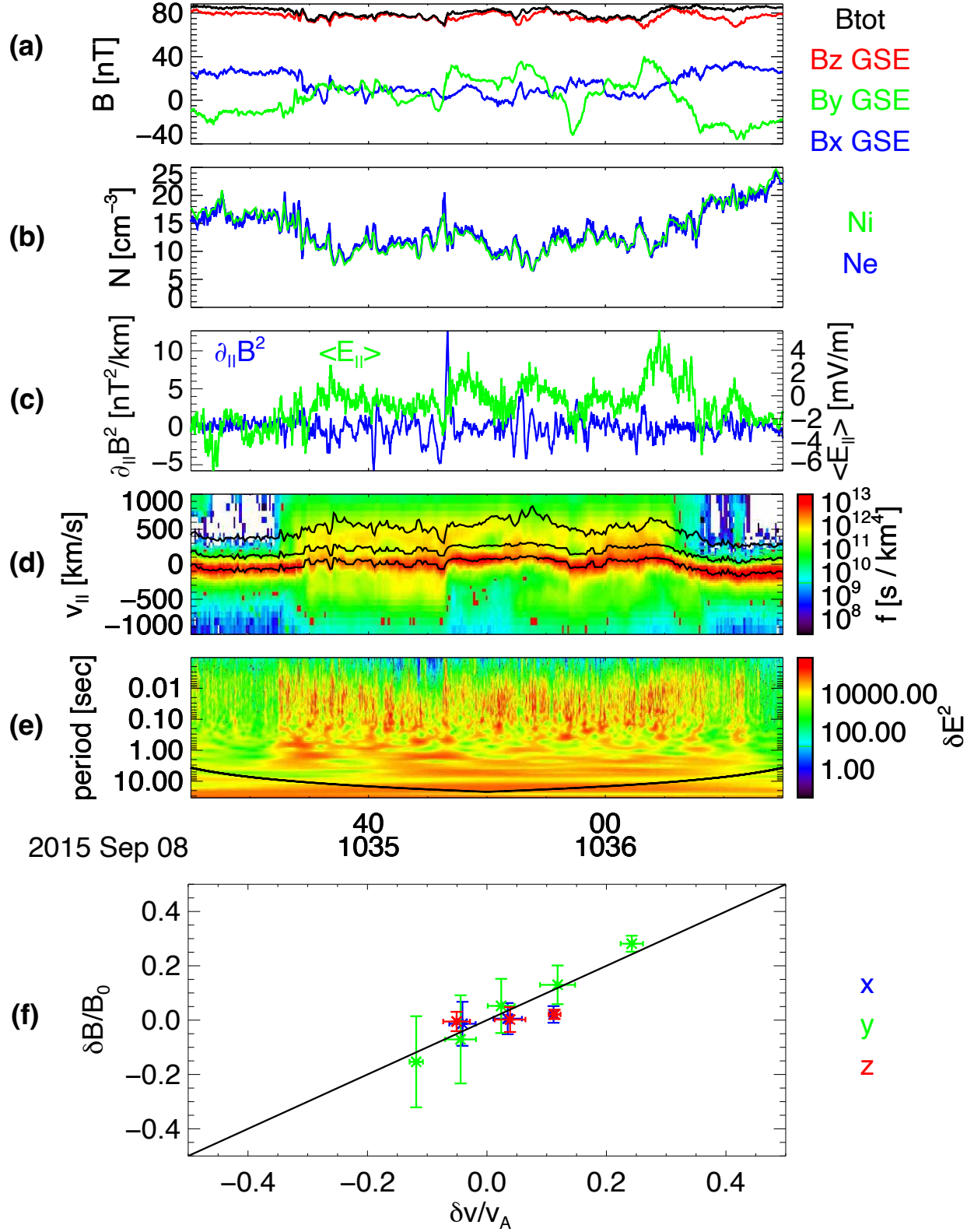
Despite the importance of Alfvén-acoustic energy channeling, direct observational evidence of this process has been difficult to obtain, mainly because of the instrumentation required to resolve ion velocity distributions at a high time cadence, as well as the vast scale separation between Alfvén waves and IAWs. In this Letter, we test the hypothesis of electrostatic-driven, cross-scale energy transfer from Alfvén waves to IAWs using the Earth’s magnetopause boundary layer as a natural laboratory, where the solar wind interaction with magnetosphere generates a plethora of large-amplitude Alfvén waves. The four-satellite Magnetospheric Multiscale (MMS) mission [28] provides simultaneous measurements for fluid-scale Alfvén waves (spatial scales resolved by inter-spacecraft interferometry), kinetic-scale IAWs (spatial scales resolved by inter-antenna interferometry with a single spacecraft), and ion velocity distributions (enabled by 3D measurements of ion velocity space with a high time resolution). The interpretation of these data is supported by event-oriented kinetic simulations.

On 8 September 2015, the MMS constellation traversed from the duskside magnetosphere to the magnetosheath between 09:10 and 11:40 UT. A surface wave, generated by the Kelvin-

Helmholtz instability, is seen through repetitive crossings of current sheets, which separate the relatively cold, dense magnetosheath from the hot, tenuous magnetopause boundary layer [29]. Thanks to the long interval (~ 80 minutes) of continuous burst-mode data collected during boundary layer crossing, a rich variety of complex plasma dynamics was observed, including Alfvénic turbulence [30], ion beams and plasma heating [31], and large-amplitude (~ 100 mV/m) electrostatic waves [32].

Figure 1 shows an example of magnetopause crossings between 10:35:35 and 10:36:05 UT (see Supplemental Materials [33] for the whole event of magnetopause crossing). Within the magnetopause boundary layer, enhanced Alfvén waves with a normalized amplitude $|\delta B/B_0| \sim 0.2$ are identified by the correlated perturbations between magnetic and velocity fields, as shown in Figure 1(f). Here B_0 is the background magnetic field averaged in the magnetopause boundary layer. The magnetic field data from the four MMS spacecraft show clear time shifts among them, due to wave propagation and plasma flows. Using four-spacecraft interferometry (see explanations in Supplemental Materials [34]), we determine the parallel wave propagation velocity to be 539 km/s $\approx v_A$ in the plasma rest frame and the corresponding wavelength to be 2059 km $\approx 30 d_i$ for the dominant frequency 0.05 Hz = $0.05 f_{ci}$ in the spacecraft frame (0.26 Hz = $0.26 f_{ci}$ in the plasma rest frame). Here, $d_i = 68$ km, $f_{ci} = 1$ Hz and $v_A = 506$ km/s are the ion inertial length, ion gyrofrequency and Alfvén velocity, respectively, averaged over the interval 10:35:40–10:36:00 UT. These large-amplitude Alfvén waves steepen into current sheets with strong gradients in the total magnetic field (e.g., around 10:35:46 UT), which are colocated with density bumps and low-frequency parallel electric fields [Figures 1(b) and 1(c)]. Such density and electric field perturbations are likely driven by gradients in the wave magnetic-field pressure [Figure 1(c)], and can be viewed as the ion acoustic mode in the long-wavelength limit [6].

Ion beams (local maximums in phase space density in v_{\parallel} aside from the ion core) are seen in the reduced velocity distributions at variable parallel velocities up to $v_A = 506$ km/s relative to the ion core [Figure 1(d)]. These ion beams are believed to be driven by resonant interactions between ions and Alfvénic fluctuations [31]. Intense broadband electrostatic waves appear during each boundary layer crossing throughout the ~ 2 -hour event [Figure 1(e)], with frequencies ranging from 10 Hz to the ion plasma frequency $f_{pi} = 700$ Hz. Identified as the ion acoustic mode, these waves are likely excited by the ion beams [32]. By analyzing time delays between the voltage signals in each pair of opposing voltage-sensitive



probes in three orthogonal directions (with tip-to-tip effective distances of 120 m in the spin plan and 30 m along the spin axis), we perform interferometry for short-wavelength IAWs at

FIG. 1. An example of magnetopause boundary layer crossing by MMS1 on 8 September 2015. The boundary layer is observed between 10:35:33 and 10:36:08 UT. (a) Three components of magnetic field in Geocentric Solar Ecliptic (GSE) coordinate system measured by the Fluxgate Magnetometer at 128 Samples/second [35]. The total magnetic field strength is shown in black. (b) Ion and electron densities measured by the Fast Plasma Investigation (FPI) instrument at time cadences of 150 ms and 30 ms, respectively [36]. (c) Parallel spatial gradients of magnetic field pressure and smoothed parallel electric fields. (d) Reduced ion parallel velocity distributions obtained from integrating phase space densities measured in the 3D velocity space (energy, pitch angle, gyrophase) by the FPI instrument. The phase space density is coded in color. The three solid lines from top to bottom indicate Alfvén and ion acoustic velocities relative to the ion core, and the maximum phase space density at each time, respectively. (e) Wavelet analysis of electric field measured by the Electric Double Probes at a sampling rate 8192 Samples/second [37, 38]. The spectral density is coded in color. The black line tracks the cone of influence, below which the stretched wavelets extend beyond the edges of the observation interval. (f) Correlated magnetic and plasma flow perturbations for the interval 10:35:35–10:36:05 UT. The magnetic field is normalized by the mean magnetic field of this interval. The plasma flow velocity is normalized by the mean Alfvén velocity of this interval. The x , y and z components of each perturbation is color-coded in blue, green, and red.

various locations in the boundary layer (see analysis in Supplemental Materials [39]). The IAWs propagate within 15° relative to B_0 or $-B_0$, with phase speeds $0.1\text{--}1.5 c_s$ in the plasma rest frame. They have wavelengths of $1\text{--}30 \lambda_D$, where c_s is the ion acoustic velocity and λ_D the local Debye length. The antiparallel-propagating IAWs are consistent with ion beams in the antiparallel direction, although these beams are weaker than those in the parallel direction.

It is important to determine the ordering of ion acoustic and Alfvén velocities, c_s and v_A , relative to the thermal velocity of core ions v_{Ti} (excluding beam ions). The electron-to-ion temperature ratio is $T_e/T_i \approx 0.25$, and the ion beta is $\beta_i = n_0 T_i / (B_0^2 / 8\pi) \approx 0.15$, which yields $c_s/v_{Ti} = \sqrt{(5/3) + (T_e/T_i)} \approx 1.4$ and $v_A/v_{Ti} = \sqrt{2/\beta_i} \approx 3.7$. Here, n_0 is the background density averaged in the magnetopause boundary layer. Thus, the ion beams at $v_A = 3.7v_{Ti} = 506 \text{ km/s}$ (i.e., the tail of the velocity distribution) cannot be in Landau-

resonance with the IAWs propagating along the field at $c_s = 1.4v_{Ti} = 191$ km/s (i.e., the core of the velocity distribution). Nevertheless, there must be some ion beams present at c_s to drive the IAWs; otherwise, those waves would be heavily damped by thermal core ions through Landau damping. This expectation is strongly supported by the presence of ion beams at ~ 200 km/s relative to the ion core in Figure 1(d).

To facilitate the interpretation of *in situ* observation data, we perform event-oriented kinetic simulations using the Hybrid-VPIC code [40, 41]. This code treats ions as kinetic particles and electrons as a massless fluid. Our simulation spans two dimensions [$0 \leq x \leq 120 d_i, 0 \leq y \leq 15 d_i$] in configuration space and three dimensions (v_x, v_y, v_z) in velocity space. The cell size is $\Delta x = \Delta y = 0.059 d_i$. The time step is $\Delta t = 0.004 \omega_{ci}^{-1}$ for particle push, which is divided to 10 substeps for the field solver to satisfy the Courant condition $(\Delta t/10) \cdot \omega_{ci} < (\Delta x/d_i)^2/\pi$ for the fastest eigenmode, the whistler mode. Periodic boundary conditions are applied to both fields and particles. All numerical values for fields and particles are based on MMS observations in Figure 1. A uniform background magnetic field B_0 is applied along the $+x$ direction. Initially, the system is perturbed by a spectrum of parallel-propagating Alfvén waves prescribed by $\delta B_x = 0$, $\delta B_y = -\delta B_\perp \sum_{m=3}^5 \sin(2\pi m x/L_x + \phi_i)$, and $\delta B_z = \delta B_\perp \sum_{m=3}^5 \cos(2\pi m x/L_x + \phi_i)$, where $\delta B_\perp/B_0 = 0.15$ is the wave amplitude, L_x is the system size in the x direction, and m is the mode number. The initial wave phases are uniformly distributed between 0 and 2π as $\phi_1 = 0$, $\phi_2 = 2\pi/3$, and $\phi_3 = 4\pi/3$. Ions are initialized as a drifting Maxwellian with thermal velocity $v_{Ti} = 0.27 v_A$ and perturbed transverse fluid velocities commensurate with Alfvén waves, $\delta v_x = 0$, $\delta v_y = \delta v_\perp \sum_{m=3}^5 \sin(2\pi m x/L_x + \phi_i)$, and $\delta v_z = -\delta v_\perp \sum_{m=3}^5 \cos(2\pi m x/L_x + \phi_i)$, where $\delta v_\perp/v_A \approx \delta B_\perp/B_0 = 0.15$. The uniform ion density n_0 at $t = 0$ is sampled by 400 particles in each cell. The electron-to-ion temperature ratio is 0.25. Because the electron thermal velocity is much greater than the Alfvén and ion acoustic velocities, the equation of state for electrons is isothermal, i.e., $T_e = \text{constant}$. The results are presented in normalized units: time to ω_{ci}^{-1} , lengths to d_i , velocities to v_A , densities to n_0 , electric fields to $v_A B_0/c$ (where c is the speed of light), and magnetic fields to B_0 .

The large-amplitude, broadband Alfvén waves naturally exhibit magnitude modulations, leading to phase-steepened wavefronts (see Figure 2(a) and Refs. [42, 43]). At these steepened wavefronts, rotational discontinuities are observed in the rapid phase changes of B_y and B_z over a distance of $\sim 5 d_i$ [Figure 3(a)]. The gradients of magnetic pressure drive

compressive perturbations, as described by [6]

$$\frac{\partial^2 \delta \rho}{\partial t^2} - c_s^2 \frac{\partial^2 \delta \rho}{\partial x^2} = \frac{1}{8\pi} \frac{\partial (\delta B_\perp)^2}{\partial x}, \quad (1)$$

where $\delta \rho$ is the mass density perturbation, and δB_\perp is the perpendicular magnetic field of the Alfvén waves. Consequently, a density bump of $\delta \rho / \rho_0 \lesssim 0.5$ forms at the steepened wavefront, accompanied by a parallel ion flow with a streaming velocity $\delta v / v_A = \delta \rho / \rho_0 \lesssim 0.5$ [at $x \approx 15 d_i$ in Figures 3(a)]. The relative streaming between core ions and electrons along the magnetic field are unstable to the Buneman or current-driven instability [44, 45], and are expected to generate IAWs with a maximum growth rate at the wavelength $\lambda \sim c_s / \omega_{pi} = \lambda_D \sqrt{(5T_i / 3T_e) + 1} = 2.7 \lambda_D$. Indeed, short-wavelength IAWs are observed near the steepened wavefront, appearing as short packets with spiky electric fields [Figure 3(a)]. The expected wavelength is consistent with that measured by MMS (1–30 λ_D) [46].

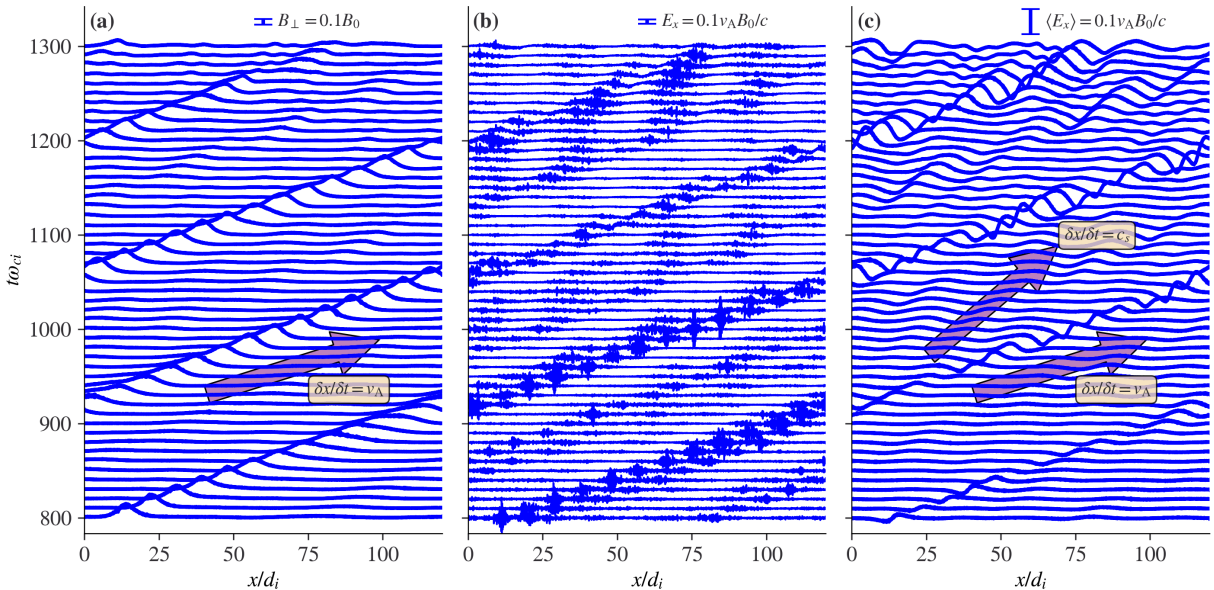


FIG. 2. Propagation characteristics of Alfvén waves and IAWs in the spatiotemporal domain in the simulation. The horizontal axis represents the x direction parallel to B_0 . The vertical axis represents time. The amplitudes of oscillations are shown at the top of each panel. (a) The perpendicular magnetic field δB_\perp . (b) The full parallel electric field δE_x . (c) The parallel electric field $\langle \delta E_x \rangle$ averaged over the y direction. The short-wavelength IAWs are canceled out by averaging in the y direction, whereas the long-wavelength electric fields survive.

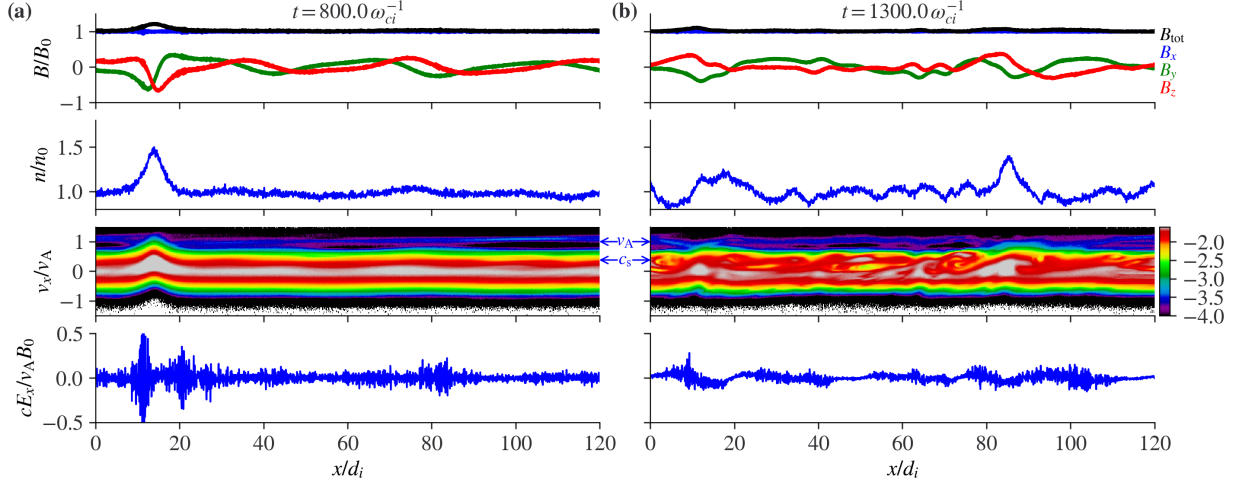


FIG. 3. The steepened Alfvén waves and the associated ion beams and kinetic-scale IAWs in the simulation. The shown time snapshots are at (a) $t = 800 \omega_{ci}^{-1}$ and (b) $t = 1300 \omega_{ci}^{-1}$. In each snapshot, the four panels from top to bottom are (1) the three components of magnetic field and the total strength, (2) the plasma density, (3) the ion phase portrait color-coded by the phase space density, and (4) the parallel electric field, respectively. The horizontal axis for all panels are the x direction parallel to B_0 .

Equation (1) reveals two compressive modes driven by large-amplitude Alfvén waves. The first mode is a particular solution to the equation, which is localized and attached to the steepened wavefront propagating at v_A . The second mode is a solution to the homogeneous part of the equation, which is periodically emitted by the steepened wavefront once a density perturbation is established, propagating at c_s . These two modes are observed in the long-wavelength electric fields [Figure 2(c)].

The two compressive modes are also manifested in the ion phase portrait. First, the localized electrostatic field at the steepened wavefront accelerates the ion tail population to v_A through Landau resonance (see Figure 3(a) and Refs. [8–10, 47]). Second, the periodic electrostatic field propagating at $c_s = 1.4 v_{Ti} = 0.38 v_A$ traps the ion thermal population, forming beams in resonant islands through nonlinear Landau resonance (see Figure 3(b) and Ref. [47]). These beams then excite short-wavelength IAWs via the ion-ion two-stream instability, with phase velocities ranging from $c_s - \Delta v_{\text{trap}}$ to $c_s + \Delta v_{\text{trap}}$, where Δv_{trap} is the resonant island half-width. These propagation velocities align with MMS interferometry analysis. Comparing Figures 3(a) and 3(b) shows that the IAW amplitude from the current-

driven (Buneman) instability near the steepened wavefront significantly exceeds that of IAWs excited by the ion-ion two-stream instability elsewhere. Asymptotically, ion beams within resonant islands phase-mix to a plateau distribution, indicating resonant heating by Alfvén waves’ nonlinearly generated parallel electric fields. The short-wavelength IAWs persist due to this plateau distribution [10, 11], analogous to electron-acoustic solitary structures in the magnetosphere [48–51].

A comparable process linking large-scale electromagnetic and small-scale electrostatic phenomena occurs in the auroral ionosphere [52, 53]. In this context, Alfvén wave propagation through inhomogeneous auroral plasma generates parallel electric fields, potentially contributing to similar field generation in our case. Additionally, hydrodynamic filamentation instability [54, 55], arising from relative streaming between beams and background plasma, can lead to the development of smaller spatial scales within the fluid regime. However, the ultimate excitation of Debye-scale electric fields necessitates kinetic instabilities, as demonstrated in our analysis.

Figure 4 compares the electromagnetic power spectra from MMS observations and simulations. Both observed and simulated spectra transition from an electromagnetic regime with $c|\delta E|/v_A|\delta B| \sim 1$ in the low-frequency ($\omega/\omega_{ci} < 1$) or long-wavelength ($kd_i < 1$) limit, to an electrostatic one with $c|\delta E|/v_A|\delta B| \gg 1$ in the high-frequency ($\omega \lesssim \omega_{pi}$) or short-wavelength ($k\lambda_D \lesssim 1$) limit.

In the electromagnetic regime, the dominant Alfvén wave at $0.07\omega_{ci}$ from the MMS observation generates second and third harmonics at $\omega/\omega_{ci} = 0.14, 0.28$ due to phase steepening, similar to the simulation. The simulation shows that long-wavelength electrostatic field energy can be comparable to transverse electric field energy [Figures 2(a) 2(c), and 4(a)–(b)], with the ordering $\langle \delta E_x \rangle^2 \sim \delta E_\perp^2 \sim 0.01(v_A B_0/c)^2 \sim (v_A \delta B_\perp/c)^2 \ll (\delta B_\perp)^2$. However, these relatively small-amplitude, long-wavelength electrostatic fields mediate energy transfer from fluid-scale Alfvén waves to kinetic-scale IAWs and core ion heating.

In the electrostatic regime, the Debye-scale IAWs exhibit a relatively flat electric field spectrum compared to the magnetic field spectrum. In the hybrid-kinetic simulation, electrostatic energy accumulates near the grid scale due to the absence of an intrinsic Debye scale to terminate the energy transfer. Nevertheless, the transition from electromagnetic fluctuations at the fluid scale to electrostatic fluctuations at the kinetic scale is clearly demonstrated in both the observations and simulations.

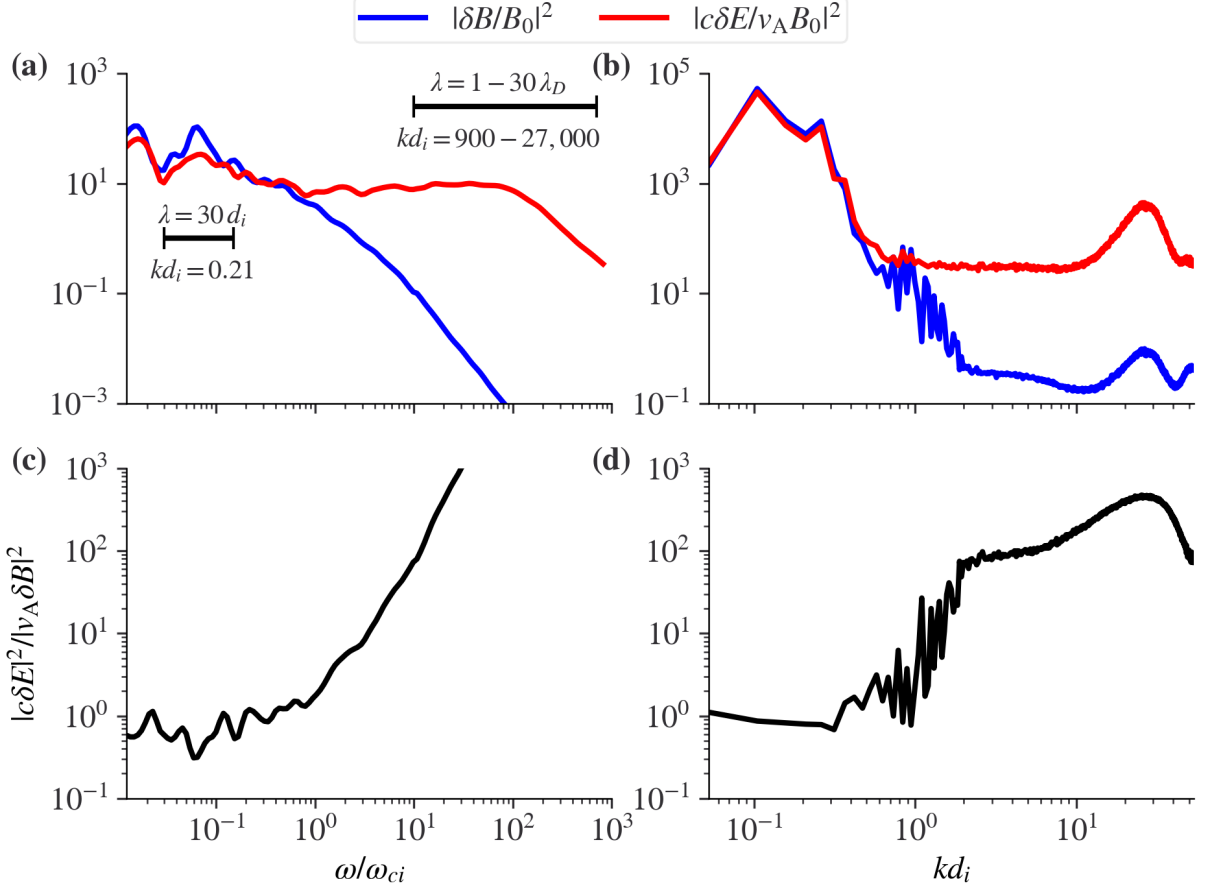


FIG. 4. Comparison of electromagnetic power spectra between the MMS observation and the simulation. (a) The electric and magnetic power spectra as functions of wave frequency and (c) the ratio between the two spectra from the MMS observation in Figure 1. Note that the shown wave frequency is in the spacecraft frame, which is Doppler-shifted from that in the plasma rest frame. There is no simple conversion between the two frequencies, because the amount of Doppler shift varies with wave frequency or wavenumber. To facilitate the mapping between wave frequencies in the spacecraft frame and wavenumbers in the plasma frame, we mark the wavenumbers of Alfvén waves and IAWs at their corresponding frequencies in the spacecraft frame. (b) The electric and magnetic power spectra as functions of wavenumber and (d) the ratio between the two spectra from the simulation at the end of the simulation $t = 1600 \omega_{ci}^{-1}$.

In summary, we provide direct observational and computational evidence supporting electrostatic-driven energy transfer from fluid-scale Alfvén waves to kinetic-scale IAWs. In a realistic parameter regime of $v_{T1} \sim c_s < v_A$, two ion beams centered at c_s and v_A are

simultaneously accelerated through nonlinear Landau resonance by two coexisting compressive electrostatic modes, both modes driven by phase-steepened Alfvén waves. This process results in the generation of kinetic-scale IAWs, substantial heating of thermal ions, and acceleration of suprathermal ions up to v_A . More broadly, the Alfvén-acoustic channelling of ion energy may contribute to ion heating near various plasma boundaries in the interplanetary space, such as magnetic discontinuities [16, 23], and low-velocity regions ahead of high-speed streams [56]. Moreover, given that the wavelengths of kinetic-scale IAWs are comparable to the electron thermal gyroradius [57, 58], the Alfvén-acoustic channelling may also contribute to the momentum exchange between ions and electrons and electron heating [21], thereby providing a collisionless dissipation mechanism to allow fast magnetic reconnection in current sheets [59–62].

ACKNOWLEDGMENTS

This work was supported by NASA grants NO. 80NSSC22K1634 and No. 80NSSC23K0086 and NSF grant NO. 2108582. We acknowledge MMS data (including FGM, EDP, and FPI) obtained from <https://lasp.colorado.edu/mms/sdc/public/>. Data access and processing was done using SPEDAS V4.1 [63]. We would like to acknowledge high-performance computing support from Derecho (<https://doi.org/10.5065/qx9a-pg09>) provided by NCAR’s Computational and Information Systems Laboratory, sponsored by the National Science Foundation [64]. We wish to thank Marco Velli for helpful discussions.

-
- [1] P. S. Iroshnikov, *Soviet Astronomy* **7**, 566 (1964).
 - [2] R. H. Kraichnan, *Physics of Fluids* **8**, 1385 (1965).
 - [3] P. Goldreich and S. Sridhar, *Astrophys. J.* **485**, 680 (1997), [astro-ph/9612243](https://arxiv.org/abs/astro-ph/9612243).
 - [4] S. Boldyrev, *Phys. Rev. Lett.* **96**, 115002 (2006).
 - [5] G. Howes, D. Drake, K. Nielson, T. Carter, C. Kletzing, and F. Skiff, *Physical review letters* **109**, 255001 (2012).
 - [6] J. V. Hollweg, *Journal of Geophysical Research* **76**, 5155 (1971).
 - [7] M. Medvedev, P. Diamond, M. Rosenbluth, and V. Shevchenko, *Physical review letters* **81**, 5824 (1998).

- [8] J. A. Araneda, E. Marsch, F. Adolfo, *et al.*, Physical review letters **100**, 125003 (2008).
- [9] L. Matteini, S. Landi, M. Velli, and P. Hellinger, Journal of Geophysical Research: Space Physics **115** (2010).
- [10] F. Valentini, P. Veltri, F. Califano, and A. Mangeney, Physical review letters **101**, 025006 (2008).
- [11] F. Valentini and P. Veltri, Physical review letters **102**, 225001 (2009).
- [12] F. Valentini, D. Perrone, and P. Veltri, The Astrophysical Journal **739**, 54 (2011).
- [13] F. Valentini, A. Vecchio, S. Donato, V. Carbone, C. Briand, J. Bougeret, and P. Veltri, The Astrophysical Journal Letters **788**, L16 (2014).
- [14] D. B. Graham, Y. V. Khotyaintsev, A. Vaivads, N. J. Edberg, A. I. Eriksson, E. P. Johansson, L. Sorriso-Valvo, M. Maksimovic, J. Souček, D. Piša, *et al.*, Astronomy & Astrophysics **656**, A23 (2021).
- [15] F. Mozer, J. Bonnell, T. Bowen, G. Schumm, and I. Vasko, The Astrophysical Journal **901**, 107 (2020).
- [16] D. Malaspina, L. Kromyda, R. Ergun, and R. Livi, AGU23 (2023).
- [17] D. M. Malaspina, R. E. Ergun, I. H. Cairns, B. Short, J. L. Verniero, C. Cattell, and R. Livi, Astrophys. J. **969**, 60 (2024).
- [18] J. Squire, B. D. Chandran, and R. Meyrand, The Astrophysical Journal Letters **891**, L2 (2020).
- [19] A. Mallet, J. Squire, B. D. Chandran, T. Bowen, and S. D. Bale, The Astrophysical Journal **918**, 62 (2021).
- [20] A. Tenerani, N. Sioulas, L. Matteini, O. Panasenco, C. Shi, and M. Velli, The Astrophysical Journal Letters **919**, L31 (2021).
- [21] F. Mozer, S. Bale, C. Cattell, J. Halekas, I. Vasko, J. Verniero, and P. Kellogg, The Astrophysical Journal Letters **927**, L15 (2022).
- [22] P. Kellogg, F. Mozer, M. Moncuquet, D. Malaspina, J. Halekas, S. Bale, and K. Goetz, The Astrophysical Journal **964**, 68 (2024).
- [23] L. Woodham, T. Horbury, L. Matteini, T. Woolley, R. Laker, S. Bale, G. Nicolaou, J. Stawarz, D. Stansby, H. Hietala, *et al.*, Astronomy & Astrophysics **650**, L1 (2021).
- [24] N. Gorelenkov, M. Van Zeeland, H. Berk, N. Crocker, D. Darrow, E. Fredrickson, G.-Y. Fu, W. Heidbrink, J. Menard, and R. Nazikian, Physics of Plasmas **16** (2009).

- [25] D. Curran, P. Lauber, P. Mc Carthy, S. da Graca, V. Igochine, A. U. Team, *et al.*, *Plasma Physics and Controlled Fusion* **54**, 055001 (2012).
- [26] A. Bierwage, N. Aiba, and K. Shinohara, *Physical Review Letters* **114**, 015002 (2015).
- [27] L. Chen and F. Zonca, *Reviews of Modern Physics* **88**, 015008 (2016).
- [28] J. L. Burch, T. E. Moore, R. B. Torbert, and B. L. Giles, *Space Sci. Rev.* **199**, 5 (2016).
- [29] S. Eriksson, B. Lavraud, F. Wilder, J. Stawarz, B. Giles, J. Burch, W. Baumjohann, R. Ergun, P.-A. Lindqvist, W. Magnes, *et al.*, *Geophysical Research Letters* **43**, 5606 (2016).
- [30] J. Stawarz, S. Eriksson, F. Wilder, R. Ergun, S. Schwartz, A. Pouquet, J. Burch, B. Giles, Y. Khotyaintsev, O. L. Contel, *et al.*, *Journal of Geophysical Research: Space Physics* **121**, 11 (2016).
- [31] L. Sorriso-Valvo, F. Catapano, A. Retinò, O. Le Contel, D. Perrone, O. W. Roberts, J. T. Coburn, V. Panebianco, F. Valentini, S. Perri, *et al.*, *Physical Review Letters* **122**, 035102 (2019).
- [32] F. Wilder, R. Ergun, S. Schwartz, D. Newman, S. Eriksson, J. Stawarz, M. Goldman, K. Goodrich, D. Gershman, D. Malaspina, *et al.*, *Geophysical Research Letters* **43**, 8859 (2016).
- [33] See Supplemental Materials for the repetitive crossings of the magnetopause boundary layer over the 2.5 hours interval, which include Refs. [28, 35–38].
- [34] See the four-spacecraft interferometry analysis of Alfvén waves in Supplemental Materials, which include Ref. [65].
- [35] C. T. Russell, B. J. Anderson, W. Baumjohann, K. R. Bromund, D. Dearborn, D. Fischer, G. Le, H. K. Leinweber, D. Leneman, W. Magnes, J. D. Means, M. B. Moldwin, R. Nakamura, D. Pierce, F. Plaschke, K. M. Rowe, J. A. Slavin, R. J. Strangeway, R. Torbert, C. Hagen, I. Jernej, A. Valavanoglou, and I. Richter, *Space Sci. Rev.* **199**, 189 (2016).
- [36] C. Pollock, T. Moore, A. Jacques, J. Burch, U. Gliese, Y. Saito, T. Omoto, L. Avanov, A. Barrie, V. Coffey, J. Dorelli, D. Gershman, B. Giles, T. Rosnack, C. Salo, S. Yokota, M. Adrian, C. Aoustin, C. Auletta, S. Aung, V. Bigio, N. Cao, M. Chandler, D. Chornay, K. Christian, G. Clark, G. Collinson, T. Corris, A. De Los Santos, R. Devlin, T. Diaz, T. Dickerson, C. Dickson, A. Diekmann, F. Diggs, C. Duncan, A. Figueroa-Vinas, C. Firman, M. Freeman, N. Galassi, K. Garcia, G. Goodhart, D. Guererro, J. Hageman, J. Hanley, E. Hemminger, M. Holland, M. Hutchins, T. James, W. Jones, S. Kreisler, J. Kujawski, V. Lavu, J. Lobell,

- E. LeCompte, A. Lukemire, E. MacDonald, A. Mariano, T. Mukai, K. Narayanan, Q. Nguyen, M. Onizuka, W. Paterson, S. Persyn, B. Piepgrass, F. Cheney, A. Rager, T. Raghuram, A. Ramil, L. Reichenthal, H. Rodriguez, J. Rouzaud, A. Rucker, Y. Saito, M. Samara, J.-A. Sauvaud, D. Schuster, M. Shappirio, K. Shelton, D. Sher, D. Smith, K. Smith, S. Smith, D. Steinfeld, R. Szymkiewicz, K. Tanimoto, J. Taylor, C. Tucker, K. Tull, A. Uhl, J. Vloet, P. Walpole, S. Weidner, D. White, G. Winkert, P.-S. Yeh, and M. Zeuch, *Space Sci. Rev.* **199**, 331 (2016).
- [37] P.-A. Lindqvist, G. Olsson, R. B. Torbert, B. King, M. Granoff, D. Rau, G. Needell, S. Turco, I. Dors, P. Beckman, J. Macri, C. Frost, J. Salwen, A. Eriksson, L. Åhlén, Y. V. Khotyaintsev, J. Porter, K. Lappalainen, R. E. Ergun, W. Vermeer, and S. Tucker, *Space Sci. Rev.* **199**, 137 (2016).
- [38] R. E. Ergun, S. Tucker, J. Westfall, K. A. Goodrich, D. M. Malaspina, D. Summers, J. Wallace, M. Karlsson, J. Mack, N. Brennan, B. Pyke, P. Withnell, R. Torbert, J. Macri, D. Rau, I. Dors, J. Needell, P.-A. Lindqvist, G. Olsson, and C. M. Cully, *Space Sci. Rev.* **199**, 167 (2016).
- [39] See Supplemental Materials for the detailed inter-antenna interferometry analysis, which include Refs. [66–68].
- [40] K. J. Bowers, B. J. Albright, L. Yin, B. Bergen, and T. J. Kwan, *Physics of Plasmas* **15** (2008).
- [41] A. Le, A. Stanier, L. Yin, B. Wetherton, B. Keenan, and B. Albright, *Physics of Plasmas* **30** (2023).
- [42] R. H. Cohen and R. M. Kulsrud, *The Physics of Fluids* **17**, 2215 (1974).
- [43] C. González, A. Tenerani, L. Matteini, P. Hellinger, and M. Velli, *The Astrophysical Journal Letters* **914**, L36 (2021).
- [44] O. Buneman, *Physical Review* **115**, 503 (1959).
- [45] R. Davidson, N. Krall, K. Papadopoulos, and R. Shanny, *Physical Review Letters* **24**, 579 (1970).
- [46] IAWs are allowed to propagate in the hybrid-kinetic scheme. However, the Debye-scale IAWs cannot be resolved in this scheme, because there is no other intrinsic, physical spatial scale in the system smaller than the ion inertial length.
- [47] C. González, M. E. Innocenti, and A. Tenerani, *Journal of Plasma Physics* **89**, 905890208 (2023).

- [48] J. P. Holloway and J. Dorning, *Physical Review A* **44**, 3856 (1991).
- [49] F. Valentini, T. M. O’Neil, and D. H. Dubin, *Physics of plasmas* **13** (2006).
- [50] X. An, J. Li, J. Bortnik, V. Decyk, C. Kletzing, and G. Hospodarsky, *Phys. Rev. Lett.* **122**, 045101 (2019).
- [51] X. An, J. Bortnik, and X.-J. Zhang, *Journal of Geophysical Research (Space Physics)* **126**, e28643 (2021).
- [52] V. Génot, P. Louarn, and F. Mottez, *J. Geophys. Res.* **106**, 29633 (2001).
- [53] V. Génot, P. Louarn, and F. Mottez, *Annales Geophysicae* **22**, 2081 (2004).
- [54] F. Mottez, G. Chanteur, and A. Roux, *Journal of Geophysical Research: Space Physics* **97**, 10801 (1992).
- [55] M. Gedalin, M. Medvedev, A. Spitkovsky, V. Krasnoselskikh, M. Balikhin, A. Vaivads, and S. Perri, *Physics of Plasmas* **17** (2010).
- [56] D. Gurnett, E. Marsch, W. Pilipp, R. Schwenn, and H. Rosenbauer, *Journal of Geophysical Research: Space Physics* **84**, 2029 (1979).
- [57] S. Kamaletdinov, I. Vasko, A. Artemyev, R. Wang, and F. Mozer, *Physics of Plasmas* **29** (2022).
- [58] S. R. Kamaletdinov, I. Y. Vasko, and A. V. Artemyev, *Journal of Plasma Physics* **90**, 905900201 (2024).
- [59] F. Coroniti and A. Eviatar, *Astrophysical Journal Supplement Series*, vol. 33, Feb. 1977, p. 189-210. **33**, 189 (1977).
- [60] R. Z. Sagdeev, *Reviews of Modern Physics* **51**, 1 (1979).
- [61] D. F. Smith and E. Priest, *Astrophysical Journal*, vol. 176, p. 487 **176**, 487 (1972).
- [62] B. Coppi and A. B. Friedland, *Astrophysical Journal*, vol. 169, p. 379 **169**, 379 (1971).
- [63] V. Angelopoulos, P. Cruce, A. Drozdov, E. W. Grimes, N. Hatzigeorgiu, D. A. King, D. Larson, J. W. Lewis, J. M. McTiernan, D. A. Roberts, C. L. Russell, T. Hori, Y. Kasahara, A. Kumamoto, A. Matsuoka, Y. Miyashita, Y. Miyoshi, I. Shinohara, M. Teramoto, J. B. Faden, A. J. Halford, M. McCarthy, R. M. Millan, J. G. Sample, D. M. Smith, L. A. Woodger, A. Masson, A. A. Narock, K. Asamura, T. F. Chang, C.-Y. Chiang, Y. Kazama, K. Keika, S. Matsuda, T. Segawa, K. Seki, M. Shoji, S. W. Y. Tam, N. Umemura, B.-J. Wang, S.-Y. Wang, R. Redmon, J. V. Rodriguez, H. J. Singer, J. Vandegriff, S. Abe, M. Nose, A. Shinbori, Y.-M. Tanaka, S. UeNo, L. Andersson, P. Dunn, C. Fowler, J. S. Halekas, T. Hara,

- Y. Harada, C. O. Lee, R. Lillis, D. L. Mitchell, M. R. Argall, K. Bromund, J. L. Burch, I. J. Cohen, M. Galloy, B. Giles, A. N. Jaynes, O. Le Contel, M. Oka, T. D. Phan, B. M. Walsh, J. Westlake, F. D. Wilder, S. D. Bale, R. Livi, M. Pulupa, P. Whittlesey, A. DeWolfe, B. Harter, E. Lucas, U. Auster, J. W. Bonnell, C. M. Cully, E. Donovan, R. E. Ergun, H. U. Frey, B. Jackel, A. Keiling, H. Korth, J. P. McFadden, Y. Nishimura, F. Plaschke, P. Robert, D. L. Turner, J. M. Weygand, R. M. Candey, R. C. Johnson, T. Kovalick, M. H. Liu, R. E. McGuire, A. Breneman, K. Kersten, and P. Schroeder, *Space Sci. Rev.* **215**, 9 (2019).
- [64] Computational and Information Systems Laboratory, “Derecho: HPE Cray EX System,” Boulder, CO: National Center for Atmospheric Research (2024).
- [65] G. Paschmann and S. Schwartz, in *Cluster-II workshop multiscale/multipoint plasma measurements*, Vol. 449 (2000) p. 99.
- [66] I. Vasko, F. Mozer, V. Krasnoselskikh, A. Artemyev, O. Agapitov, S. Bale, L. Avanov, R. Ergun, B. Giles, P.-A. Lindqvist, *et al.*, *Geophysical Research Letters* **45**, 5809 (2018).
- [67] I. Y. Vasko, R. Wang, F. S. Mozer, S. D. Bale, and A. V. Artemyev, *Frontiers in Physics* **8**, 156 (2020).
- [68] B. U. Ö. Sonnerup and L. J. Cahill, Jr., *J. Geophys. Res.* **73**, 1757 (1968).

Supplemental materials for “Cross-scale energy transfer from
fluid-scale Alfvén waves to kinetic-scale ion acoustic waves in the
Earth’s magnetopause boundary layer”

Xin An,^{1,*} Anton Artemyev,¹ Vassilis Angelopoulos,¹
Terry Z. Liu,¹ Ivan Vasko,² and David Malaspina^{3,4}

¹*Department of Earth, Planetary, and Space Sciences,
University of California, Los Angeles, CA, 90095, USA*

²*Department of Physics, University of Texas at Dallas, Richardson, TX, 75080, USA*

³*Astrophysical and Planetary Sciences Department,
University of Colorado, Boulder, CO, 80305, USA*

⁴*Laboratory for Atmospheric and Space Physics,
University of Colorado, Boulder, CO, 80303, USA*

(Dated: November 27, 2024)

Abstract

These Supplemental Materials complement the main manuscript by providing additional supporting information. The first section offers the instrumentation details alongside the event overview spanning 2.5 hours. In the second section, we delve into the characteristics of Alfvén waves, leveraging the inter-spacecraft interferometry to assess their propagation and computing spatial gradients of magnetic-field pressure associated with these waves. Finally, the third section investigates the propagation characteristics of ion acoustic waves through inter-antenna interferometry.

S1. INSTRUMENTATION AND EVENT OVERVIEW

This study utilizes three instruments aboard the Magnetospheric Multiscale (MMS) constellation [S1]: the Fluxgate Magnetometer (FGM), Electric Double Probes (EDP), and Fast Plasma Investigation (FPI). The FGM records three orthogonal components of magnetic field at a sampling rate of 128 Samples/second [S2]. The EDP, comprising Axial Double Probes (ADP) [S3] and Spin-Plane Double Probes (SDP) [S4], measures the full vector of electric field both along and perpendicular to the spin axis at a sampling rate of 8192 Samples/second. The FPI captures the 3D velocity-space distribution of electrons from 10 eV to 30 keV and ions from 10 eV to 30 keV with respective time resolutions of 30 ms, and 150 ms [S5].

We choose the magnetopause boundary layer as a natural laboratory to study the Alfvén-acoustic channeling for ion energy, where plenty of large-amplitude Alfvén waves are generated due to solar wind interactions with the magnetosphere. In addition, the ion velocity distributions are better resolved in the boundary layer than in the solar wind. Figure S1 illustrates a 2.5-hour traversal of the magnetopause boundary layer by MMS on 8 September 2015. During this period, surface waves generated by the Kelvin-Helmholtz instability manifest as oscillations in magnetic fields, flow velocities, and ion and electron energy fluxes. A 10 minute interval of the same event, from 10:30 to 10:40 UT, is depicted in Figure S2. Notably, the spacecraft alternates between traversing the relatively cold, dense magnetosheath plasma and the hot, tenuous boundary layer, separated by current sheets.

The two pivotal parameters for this study are the ion beta β_i and the electron-to-ion

* phyax@ucla.edu

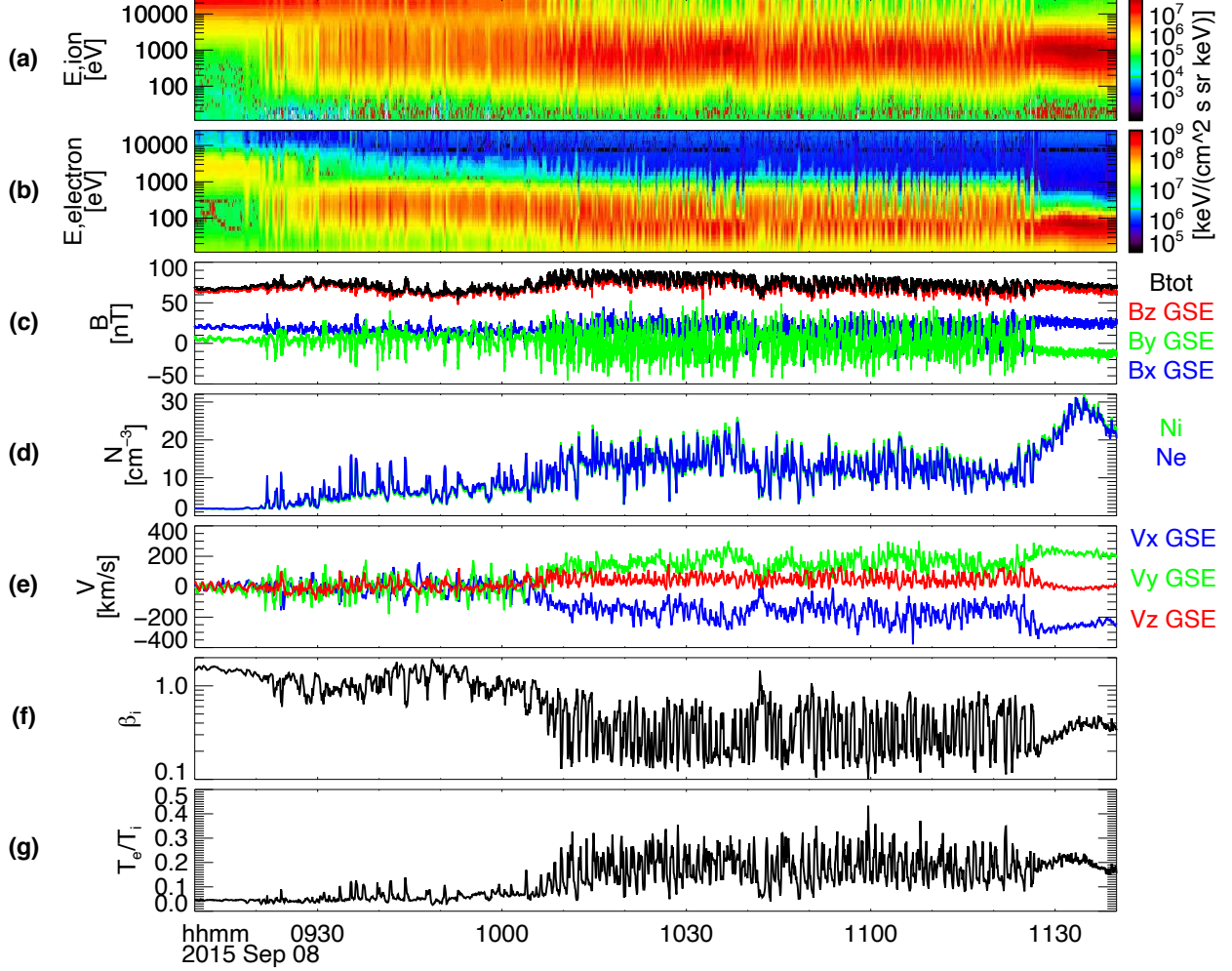


FIG. S1. Event overview of the magnetopause boundary layer crossing by MMS1 on 8 September, 2015. The MMS constellation is located around $(X, Y, Z) = (5 R_E, 8.8 R_E, 0.1 R_E)$ in the geocentric solar ecliptic (GSE) coordinate, where R_E is the Earth radius. (a) The ion energy spectrum color-coded by the ion energy flux. (b) The electron energy spectrum color-coded by the electron energy flux. (c) The three components of magnetic field in the GSE coordinate and the total magnetic field magnitude (black). (d) The ion (green) and electron (blue) densities. (e) The three components of ion flow velocity in the GSE coordinate. (f) The ion beta β_i defined as the ratio of ion thermal pressure to magnetic field pressure. (g) The electron-to-ion temperature ratio T_e/T_i .

temperature ratio T_e/T_i . It has been verified that the increase in β_i and the decrease in T_e/T_i within the boundary layer are caused by the presence of ion beams compared to the magnetosheath. Excluding beam ions, these parameters are evaluated to be $\beta_i = 0.15$ and $T_e/T_i = 0.25$. This gives the relative locations of Alfvén and ion acoustic velocities to the

thermal velocity of core ions as $v_A/v_{Ti} = \sqrt{\beta_i/2} = 3.7$ and $c_s/v_{Ti} = \sqrt{(5/3) + (T_e/T_i)} = 1.4$.

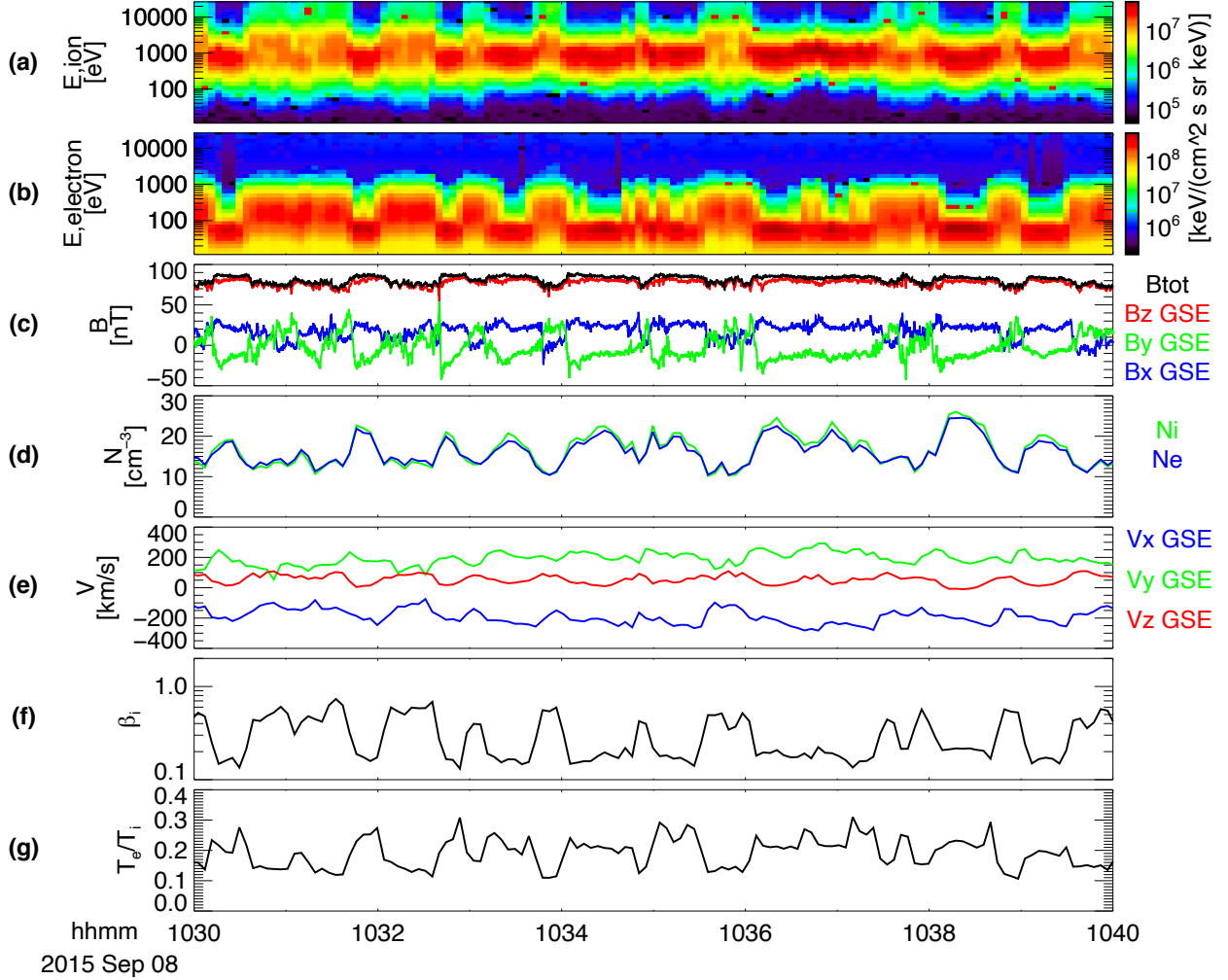


FIG. S2. Zoom-in view of the event in Figure S1 between 10:30–10:40 UT on 8 September, 2015. The interval shown in the main manuscript is between 10:35:25–10:36:15 UT.

S2. INTER-SPACECRAFT INTERFEROMETRY ANALYSIS OF ALFVÉN WAVES

A. Propagation characteristics

We analyze the propagation characteristics of Alfvén waves utilizing the four-satellite interferometry technique. Examination of the magnetic field variations of Alfvén waves observed on MMS1–MMS4 reveals distinct time lags, as depicted in Figure S3. The propagation velocity of Alfvén waves can be obtained by minimizing the sum of the squares of the

residual time between each pair of spacecraft, where the residual time refers to the difference between the measured and predicted propagation time.

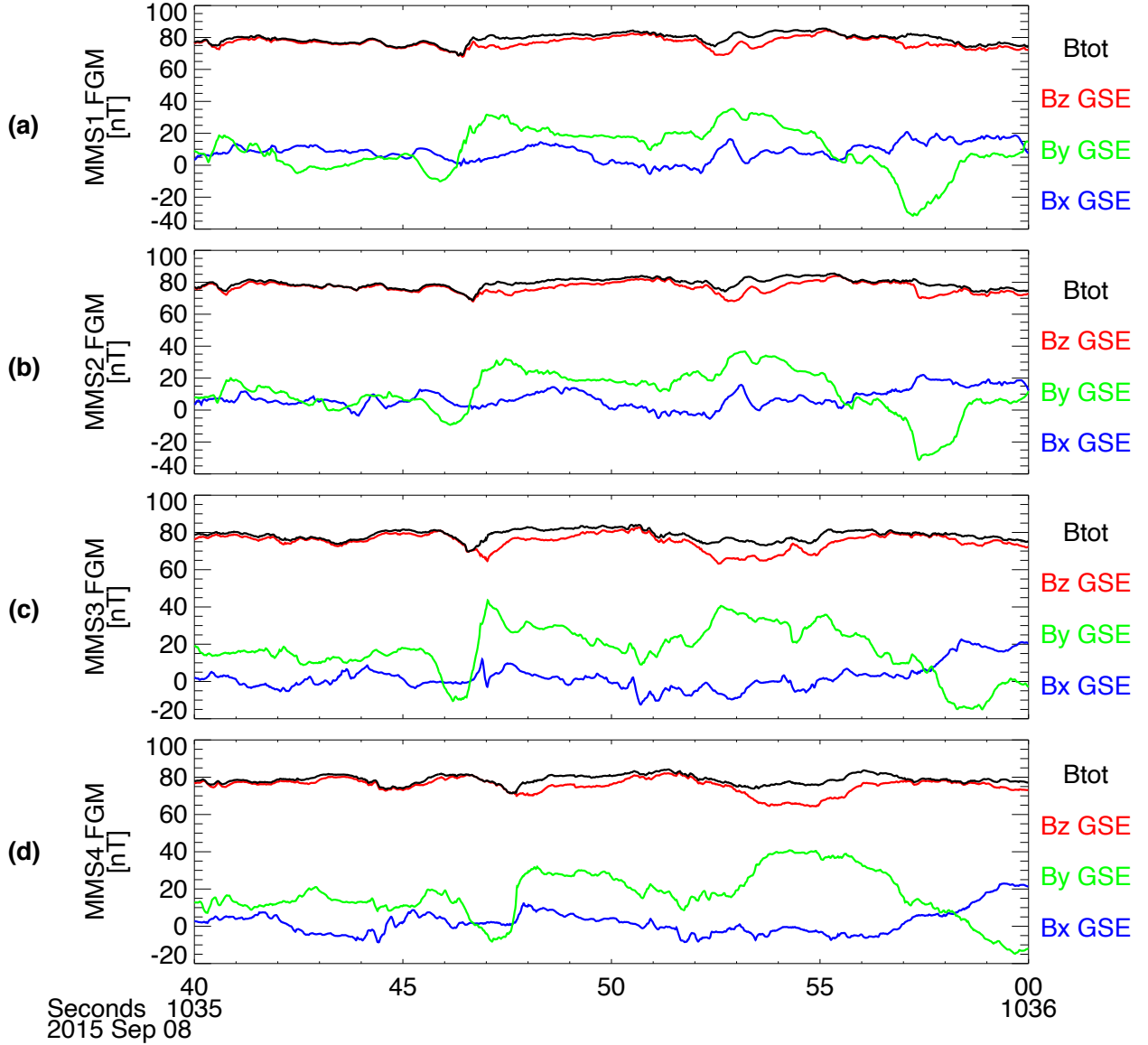


FIG. S3. The measurements of magnetic field vector by FGM onboard (a) MMS1, (b) MMS2, (c) MMS3, and (d) MMS4.

The propagation time of the magnetic field B_y between each pair of spacecraft is determined by identifying the peak of their cross-correlation coefficient as a function of time lag, as illustrated in Figure S4. B_y is selected for the analysis due to its significant variations during the event. The timings across the four spacecraft are synchronized, and the measured propagation time $t_{\alpha\beta}$ and the corresponding distance $|\mathbf{r}_\alpha - \mathbf{r}_\beta|$ between each pair of

spacecraft (α, β) are detailed in Table S1. It is worth noting that the measured propagation time may not strictly satisfy $t_{\alpha\gamma} - t_{\beta\gamma} = t_{\alpha\beta}$. Thus, we determine the propagation velocity by minimizing the cost function defined as:

$$\mathcal{C} = \sum_{\alpha \neq \beta} \left| \frac{\hat{\mathbf{n}} \cdot (\mathbf{r}_\alpha - \mathbf{r}_\beta)}{V} - t_{\alpha\beta} \right|^2, \quad (1)$$

where $\hat{\mathbf{n}}$ represents the unit vector along the propagation direction, V denotes the propagation velocity, and $\sum_{\alpha \neq \beta}$ encompasses all mutually different pairs of spacecraft listed in Table S1. This constitutes a linear optimization problem since the residual time is linear with respect to the vector $\mathbf{m} = \hat{\mathbf{n}}/V$. The solution to the linear optimization problem is given by (see Chapter 12 in Ref. [S6]):

$$m_l = \frac{1}{4^2} \sum_{\alpha \neq \beta} t_{\alpha\beta} (r_{\alpha k} - r_{\beta k}) R_{kl}^{-1}, \quad (2)$$

where $r_{\alpha k}$ represents the k -th component of the spacecraft position \mathbf{r}_α , and the volumetric tensor R_{kl} is defined as:

$$R_{kl} = \frac{1}{4} r_{\alpha k} r_{\alpha l}. \quad (3)$$

The Einstein summation convention is followed in Equations (2) and (3). Note that the origin of the coordinate system is chosen at the mean position of the four spacecraft, as the property $\sum_\alpha \mathbf{r}_\alpha = 0$ has been used in deriving Equation (2). From Equation (2), the magnitude and direction of the propagation velocity in the spacecraft frame in the GSE coordinate are determined to be

$$V = 103 \text{ km/s}, \quad \hat{\mathbf{n}} = (-0.98, -0.15, 0.1). \quad (4)$$

The dominant wave frequency in the spacecraft frame is $f = 0.05$ Hz, corresponding to the wavelength $\lambda = V/f = 2059 \text{ km} = 30 d_i$.

The propagation velocity in the plasma rest frame can be deduced from that in the spacecraft frame by considering the Doppler effect:

$$\omega = \omega' + \mathbf{k} \cdot \mathbf{u}, \quad (5)$$

where ω is the wave frequency in the spacecraft frame, ω' is the wave frequency in the plasma rest frame, \mathbf{k} is the corresponding wavenumber, and \mathbf{u} is the mean plasma flow velocity

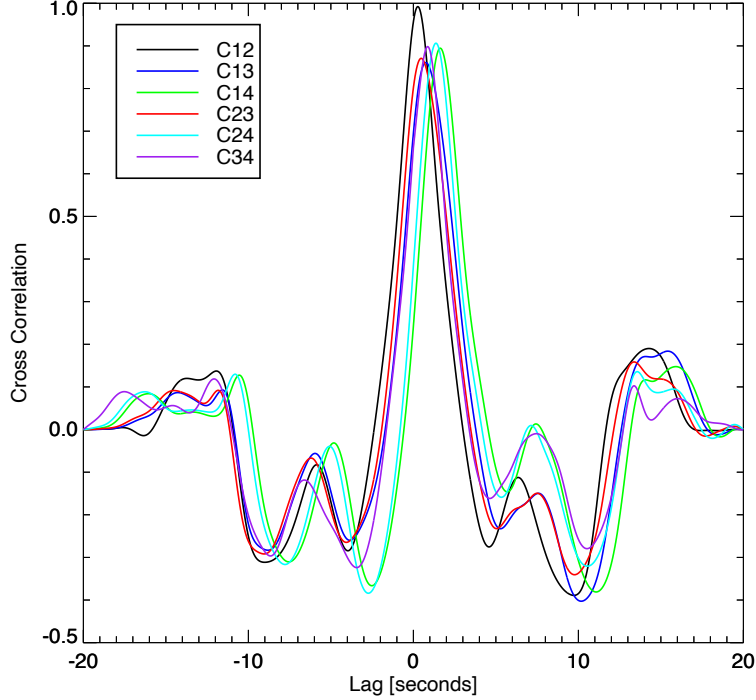


FIG. S4. Cross-correlation coefficients of B_y from six pairs of mutually different MMS spacecraft in Figure S3. The horizontal axis is the time lag. The time lag corresponding to the peak of cross-correlation coefficient is denoted as the propagation time between each pair of spacecraft.

Pair (α, β)	$t_{\alpha\beta}$ [seconds]	$ \mathbf{r}_\alpha - \mathbf{r}_\beta $ [km]
MMS2 - MMS1	0.27	153
MMS3 - MMS1	0.76	176
MMS4 - MMS1	1.63	183
MMS3 - MMS2	0.48	180
MMS4 - MMS2	1.37	166
MMS4 - MMS3	0.87	200

TABLE S1. The propagation time $t_{\alpha\beta}$ and distance between six pairs of mutually different spacecraft.

during the event. Dividing both sides of Equation (5) by k , we obtain the propagation velocity in the plasma rest frame

$$V' = V - \hat{\mathbf{n}} \cdot \mathbf{u}, \quad (6)$$

where $V' = \omega'/k$, $V = \omega/k$, and $\hat{\mathbf{n}} = \mathbf{k}/k$. By substituting the values from Equation (4)

and $\mathbf{u} = (-114, 151, 85)$ km/s into Equation (6), we find the magnitude of the propagation velocity in the plasma frame to be $V' = 5$ km/s, with the propagation direction remaining $\hat{\mathbf{n}}$. The parallel propagation velocity in the plasma rest frame is $V'_{\parallel} = \omega' / (k\hat{\mathbf{n}} \cdot \hat{\mathbf{b}}) = 539$ km/s, which is approximately equal to the Alfvén velocity.

B. Spatial gradient of magnetic-field pressure

In Figure 1(c) of the main manuscript, the spatial gradient of the magnetic-field pressure is computed using the four MMS spacecraft. Let \mathbf{k} represent this gradient:

$$\mathbf{k} = \frac{\partial B^2}{\partial \mathbf{r}}, \quad (7)$$

where \mathbf{r} denotes position. The magnetic pressure B_{α}^2 is simultaneously measured by the four MMS spacecraft ($\alpha = \text{MMS1, MMS2, MMS3, MMS4}$). We optimize the spatial gradient of B_{α}^2 by minimizing the cost function:

$$\mathcal{C} = \sum_{\alpha \neq \beta} |\mathbf{k} \cdot (\mathbf{r}_{\alpha} - \mathbf{r}_{\beta}) - (B_{\alpha}^2 - B_{\beta}^2)|^2. \quad (8)$$

Because Equation (8) has the same form as Equation (1), with $t_{\alpha\beta}$ replaced by $(B_{\alpha}^2 - B_{\beta}^2)$, the solution is similar [S6]

$$k_l = \frac{1}{4^2} \sum_{\alpha \neq \beta} (B_{\alpha}^2 - B_{\beta}^2) (r_{\alpha k} - r_{\beta k}) R_{kl}^{-1}, \quad (9)$$

where the volumetric tensor has been defined in Equation (3).

S3. INTER-ANTENNA INTERFEROMETRY ANALYSIS OF ION ACOUSTIC WAVES

We determine the propagation characteristics of ion acoustic waves using the inter-antenna interferometry technique. Figure S5 shows an example of the three components of electric field in the boom directions, computed as $E_{ij} = c_{ij}(V_i - V_j)/(2l_{ij})$. Here, V_i and V_j are the voltage signals from two opposing voltage-sensitive probes with a length l_{ij} , and the correction factors c_{ij} account for the sensor frequency response and finite boom length [S7]. The voltage signals of V_1 vs. $-V_2$, V_3 vs. $-V_4$, and V_5 vs. $-V_6$ are in the three orthogonal directions. The physical length between the voltage sensors in the spin plane

is $2l_{12} = 2l_{34} = 120$ m, whereas the physical length along the spin axis is $2l_{56} = 29.2$ m. The time delays between voltage signals between opposing probes allow us to determine the magnitude and direction of the propagation velocity as follows [S7, S8]:

$$\frac{1}{V_s^2} = \frac{\Delta t_{12}^2}{l_{12}^2} + \frac{\Delta t_{34}^2}{l_{34}^2} + \frac{\Delta t_{56}^2}{l_{56}^2}, \quad (10)$$

$$\hat{\mathbf{k}} = \left(-\frac{V_s \Delta t_{12}}{l_{12}}, -\frac{V_s \Delta t_{34}}{l_{34}}, -\frac{V_s \Delta t_{56}}{l_{56}} \right). \quad (11)$$

We find that the propagation velocity is 270 km/s in the spacecraft frame and 82 km/s in the plasma rest frame, which is approximately equal to the local ion acoustic velocity 90 km/s. The propagation angle is within 10° relative to the local magnetic field direction and is aligned with the electric field direction, indicating that the observed electric field is approximately a one-dimensional electrostatic structure. The estimated propagation velocity and the one-dimensional nature of the electric field structures allow us to translate their temporal profiles to spatial profiles, as shown in Figure S6. The electrostatic potential is calculated as $\Phi = \int E_l V_s dt$, where E_l is the dominant electric field determined using minimum variance analysis [S9]. The amplitude of the electrostatic potential is about 0.5 Volts. The wavelength is 400 m $\approx 13 \lambda_D$, where $\lambda_D = 30$ m is the local Debye length. The propagation characteristics of ion acoustic waves at several other times are listed in Table S2. At times, ion acoustic waves also propagate antiparallel to B_0 , excited by ion beams with $v_{\parallel} < 0$, likely caused by parts of resonant islands extending to the antiparallel direction.

[S1] J. L. Burch, T. E. Moore, R. B. Torbert, and B. L. Giles, Magnetospheric Multiscale Overview and Science Objectives, *Space Sci. Rev.* **199**, 5 (2016).

[S2] C. T. Russell, B. J. Anderson, W. Baumjohann, K. R. Bromund, D. Dearborn, D. Fischer, G. Le, H. K. Leinweber, D. Leneman, W. Magnes, J. D. Means, M. B. Moldwin, R. Nakamura, D. Pierce, F. Plaschke, K. M. Rowe, J. A. Slavin, R. J. Strangeway, R. Torbert, C. Hagen, I. Jernej, A. Valavanoglou, and I. Richter, The Magnetospheric Multiscale Magnetometers, *Space Sci. Rev.* **199**, 189 (2016).

[S3] R. E. Ergun, S. Tucker, J. Westfall, K. A. Goodrich, D. M. Malaspina, D. Summers, J. Wallace, M. Karlsson, J. Mack, N. Brennan, B. Pyke, P. Withnell, R. Torbert, J. Macri, D. Rau, I. Dors,

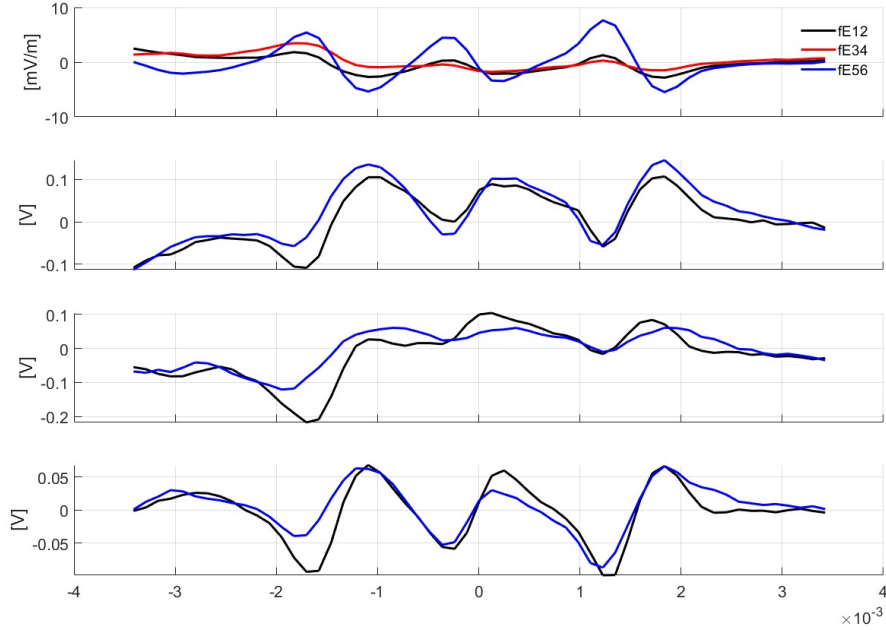


FIG. S5. The electric field and associated voltage signals in three pairs of opposing voltage-sensitive probes. (a) The three orthogonal components of electric field in the spin plane and along the spin axis. (b), (c) The voltage signals V_1 vs. $-V_2$ and V_3 vs. $-V_4$ in the two perpendicular directions in the spin plane. (d) The voltage signals V_5 vs. $-V_6$ along the spin axis. The time zero is at 10:35:46.6 UT on 8, September, 2015. Each division is 1 ms on the horizontal axis.

J. Needell, P.-A. Lindqvist, G. Olsson, and C. M. Cully, The Axial Double Probe and Fields Signal Processing for the MMS Mission, *Space Sci. Rev.* **199**, 167 (2016).

[S4] P.-A. Lindqvist, G. Olsson, R. B. Torbert, B. King, M. Granoff, D. Rau, G. Needell, S. Turco, I. Dors, P. Beckman, J. Macri, C. Frost, J. Salwen, A. Eriksson, L. Åhlén, Y. V. Khotyaintsev, J. Porter, K. Lappalainen, R. E. Ergun, W. Wernmeier, and S. Tucker, The Spin-Plane Double Probe Electric Field Instrument for MMS, *Space Sci. Rev.* **199**, 137 (2016).

[S5] C. Pollock, T. Moore, A. Jacques, J. Burch, U. Gliese, Y. Saito, T. Omoto, L. Avanov, A. Barrie, V. Coffey, J. Dorelli, D. Gershman, B. Giles, T. Rosnack, C. Salo, S. Yokota, M. Adrian, C. Aoustin, C. Aulletti, S. Aung, V. Bigio, N. Cao, M. Chandler, D. Chornay, K. Christian, G. Clark, G. Collinson, T. Corris, A. De Los Santos, R. Devlin, T. Diaz, T. Dickerson, C. Dickson, A. Diekmann, F. Diggs, C. Duncan, A. Figueroa-Vinas, C. Firman, M. Freeman, N. Galassi, K. Garcia, G. Goodhart, D. Guererro, J. Hageman, J. Hanley, E. Hemminger, M. Holland, M. Hutchins, T. James, W. Jones, S. Kreisler, J. Kujawski, V. Lavu, J. Lobell,

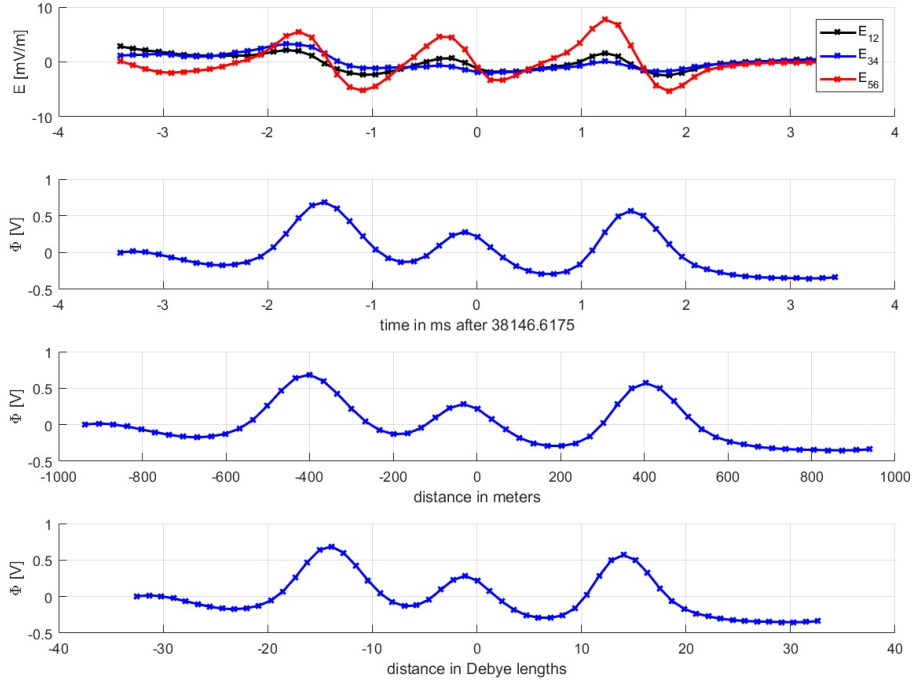


FIG. S6. The translation of electric field as a function of time in Figure S5 to electrostatic potential as a function of position. (a) The temporal profiles of electric field in the spin plane and along the spin axis. (b) The temporal profile of electrostatic potential. (c), (d) The spatial profiles of electrostatic potential in meters and normalized to the local Debye length.

E. LeCompte, A. Lukemire, E. MacDonald, A. Mariano, T. Mukai, K. Narayanan, Q. Nguyen, M. Onizuka, W. Paterson, S. Persyn, B. Piepgrass, F. Cheney, A. Rager, T. Raghuram, A. Ramil, L. Reichenthal, H. Rodriguez, J. Rouzaud, A. Rucker, Y. Saito, M. Samara, J.-A. Sauvaud, D. Schuster, M. Shappirio, K. Shelton, D. Sher, D. Smith, K. Smith, S. Smith, D. Steinfeld, R. Szymkiewicz, K. Tanimoto, J. Taylor, C. Tucker, K. Tull, A. Uhl, J. Vloet, P. Walpole, S. Weidner, D. White, G. Winkert, P.-S. Yeh, and M. Zeuch, Fast Plasma Investigation for Magnetospheric Multiscale, *Space Sci. Rev.* **199**, 331 (2016).

[S6] G. Paschmann and S. Schwartz, Issi book on analysis methods for multi-spacecraft data, in *Cluster-II workshop multiscale/multipoint plasma measurements*, Vol. 449 (2000) p. 99.

[S7] I. Vasko, F. Mozer, V. Krasnoselskikh, A. Artemyev, O. Agapitov, S. Bale, L. Avanov, R. Ergun, B. Giles, P.-A. Lindqvist, *et al.*, Solitary waves across supercritical quasi-perpendicular shocks, *Geophysical Research Letters* **45**, 5809 (2018).

	Time [UT]	V_{sc} [km/s]	V' [km/s]	V'/c_s	θ_{kB} [°]	λ [m]	λ/λ_D	Φ_{max} [Volts]
MMS1	10:35:46.6	270	82	0.4	9.5	400	13	0.5
MMS1	10:35:48.5	62	-46	-0.24	172	200	8	0.2
MMS1	10:35:48.58	100	14	0.07	6	100	4	0.2
MMS1	10:35:56.3	-200	-135	-0.7	174	800	27	0.3
MMS1	10:35:54.75	124	250	1.3	10	100	3	0.05
MMS2	10:35:41.26	-120	-50	-0.26	177	200	10	0.4
MMS2	10:35:43.3	-44	-12	-0.06	175	200	10	0.2
MMS2	10:35:54.46	-53	-230	-1.2	168	50	1	0.2
MMS2	10:35:55.37	-79	-11	-0.06	174	200	10	0.2
MMS2	10:35:55.9	-84	23	0.12	11	400	30	0.2

TABLE S2. Propagation characteristics of ion acoustic waves measured by MMS1 and MMS2. V_{sc} and V' represent the propagation velocity of ion acoustic waves in the spacecraft and plasma rest frames, respectively. θ_{kB} represents the angle between the propagation direction and the magnetic field direction. λ represents the wavelength. Φ_{max} represents the maximum amplitude of the electrostatic potential. c_s is the ion acoustic velocity. λ_D is the local Debye length. The propagation characteristics of ion acoustic waves measured by MMS3 and MMS4 are similar to those observed by MMS1 and MM2.

[S8] I. Y. Vasko, R. Wang, F. S. Mozer, S. D. Bale, and A. V. Artemyev, On the nature and origin of bipolar electrostatic structures in the earth's bow shock, *Frontiers in Physics* **8**, 156 (2020).

[S9] B. U. Ö. Sonnerup and L. J. Cahill, Jr., Explorer 12 observations of the magnetopause current layer, *J. Geophys. Res.* **73**, 1757 (1968).